Chinese Physics B

Nontrivial Band Topology in β-$IrSn_4$ Superconductor revealed by de Haas–van Alphen Oscillations

To cite this article before publication: Haisen Liu *et al* 2026 *Chinese Phys. B* in press https://doi.org/10.1088/1674-1056/ae5789

Nontrivial Band Topology in β-$IrSn_4$ Superconductor revealed by de Haas–van Alphen Oscillations

Haisen Liu(刘海森)[1,2,*], Zhen Zhao(赵振)[2,*], Tianqi Gao(高天奇)[3], Ruwen Wang(王汝文)[2,3], Senhao Lv(吕森浩)[2], Guojing Hu(胡国静)[3], Jingyuan Qu(曲靖远)[2], Jianchen Lu(卢建臣)[1,†], Hui Guo(郭辉)[2,3,†], Wu Zhou(周武)[3], Haitao Yang(杨海涛)[2,3], Hong-Jun Gao(高鸿钧)[2,3]

[1] *Faculty of Materials Science and Engineering, Kunming University of Science and Technology, Kunming 650093 China*
[2] *Beijing National Center for Condensed Matter Physics and Institute of Physics, Chinese Academy of Sciences, Beijing 100190, China*
[3] *School of Physical Sciences, University of Chinese Academy of Sciences, Beijing 100049, China*

Determining the topological nature of superconductors is essential for exploring the realization of the topological superconductivity, which is considered promising for the next-generation quantum computing and novel electronic devices. However, the topological character in β-$IrSn_4$, a superconductor with a superconducting transition temperature $T_c \approx 1.1$ K, remains unexplored. In this study, we report the quantum oscillations evidence for the nontrivial band topology in β-$IrSn_4$ revealed by de Haas–van Alphen measurements (dHvA) under low-temperature and high-magnetic-field. Fourier transform analysis reveals multiple peaks (7 - 250 T), indicating the complex topology of the Fermi surface. In addition, nonzero Berry phases, determined from the Landau fan diagram, demonstrate the nontrivial band topology in β-$IrSn_4$. These findings suggest that β-$IrSn_4$ may provide a promising platform for investigating the interplay between the superconductivity and nontrivial band topology.

Keywords: Quantum oscillations, Nontrivial band topology
PACS: 71.18.+y, 74.70.-b, 74.25.-q

* These authors contributed equally to this work.
† Corresponding author. E-mail: guohui@iphy.ac.cn
† Corresponding author. E-mail: jclu@kust.edu.cn

1. Introduction

In recent years, topological materials have attracted great interest owing to the presence of non-trivial bands protected by topological invariants.[1] Such protection renders the band structure highly robust against disorder and perturbations, giving rise to a wide range of emergent quantum phenomena, including quantum Hall effects, topological insulators and Dirac semimetals.[2-4] Consequently, topological materials provide versatile platforms for both fundamental physics research and the development of advanced functional devices.[5] In many systems, topologically nontrivial bands are associated with Dirac- or Weyl-like quasiparticles and are characterized by a Berry phase close to π, leading to low-scattering, nearly loss-free, and high-mobility electronic transport properties.[6] When such topological electronic states coexist with the superconductivity, Majorana zero modes or a topological superconducting phase may emerge, offering an ideal platform for exploring the unconventional superconductivity and its application in fault-tolerant quantum computing.[7] Therefore, systematic identification and experimental verification of topological band structures in superconducting metals have become a frontier topic in condensed-matter physics.

The topological character of electronic bands can be reflected in the geometry of the Fermi surface.[8] Consequently, the dHvA effect serves as a powerful probe for elucidating both the Fermi surface topology and the underlying electronic band structure. By analyzing the dHvA oscillations using the Lifshitz–Kosevich (L-K) formalism, key quasiparticle parameters, including the effective mass and Dingle temperature (T_D), can be quantitatively extracted.[9] Moreover, the intercept of the Landau-level fan diagram allows the determination of the Berry phase, with a value close to π being widely regarded as an experimental hallmark of the nontrivial band topology.[10] Owing to their complex electronic structures and rich exotic phenomena, intermetallic compounds provide a fertile platform for exploring the superconductivity, nontrivial band topology, and unconventional transport properties.[11-13] In the topological superconductor candidate $AuSn_4$, surface superconductivity with unconventional pairing characteristics has been reported, while Rashba-type band splitting and vortex zero modes have been visualized.[14, 15] In addition, the superconductivity accompanied by the possible nontrivial band topology has been observed in $PtPb_4$.[16] β-$IrSn_4$, with a similar crystal structure of $AuSn_4$ and $PtPb_4$, exhibits superconductivity with $T_c \approx 1.1$ K.[17] However, its Fermi surface geometry and the possible nontrivial topological nature have not been experimentally established yet, and systematic dHvA studies are still required to clarify its electronic structure.

In our work, we performed dHvA measurements on high-quality β-$IrSn_4$ single crystals under low-temperature (1.9~30 K) and high magnetic field (up to 9 T). Clear quantum oscillations as a function of $1/B$ were observed under magnetic fields applied both along crystallographic c-axis ($B \parallel c$) and within the ab plane ($B \parallel ab$ plane). Fast

Fourier transform (FFT) analysis reveals several branches ($F \approx 7$~250 T), reflecting a complex geometry of Fermi surface, whose cyclotron effective masses extracted from L-K fits lie between 0.05 and 0.30 m_e. These small effective masses suggest high carrier mobility and are indicative of linear (Dirac- or Weyl-like) band dispersion or other nontrivial topological characteristics. Most importantly, the Landau-level fan diagram constructed from the dominant oscillations branch yields a Berry phase $\varphi_B \approx \pi$, providing an experimental evidence for a nontrivial topological character of the Fermi surface. Notably, the ε branch not only exhibits an exceptionally small cyclotron effective mass of merely $0.071 m_e$, but also yields a Berry phase $\varphi_B \approx 1.02\ \pi$, consistent with Dirac-like quasiparticles and a nontrivial band topology.[18-20] Furthermore, by rotating the field ($\theta = 0°$~$90°$), we carried out a systematic angle-dependent dHvA analysis, the result indicates that the Fermi surface corresponding to F_α, F_β, F_ξ and F_ε has a quasi-2D or prolate ellipsoid shape.[21] These results provided compelling experimental evidence that β-$IrSn_4$ may host the quasi-2D Fermi surface and topological electronic states. Our findings established β-$IrSn_4$ as a promising platform for exploring the interplay between the superconductivity and band topology.

2. Experimental methods

The β-$IrSn_4$ single crystals were grown by a self-flux method.[22-24] High-purity iridium powder (Alfa, 99.99 %) and tin granules (Alfa, 99.999 %) were mixed in an atomic ratio of 1: 80 and sealed under vacuum. The mixture was heated to high temperature to ensure complete dissolution, then slowly cooled to promote crystal growth, followed by a rapid cooling step to suppress the formation of the impurity α-$IrSn_4$ phase. The crystals were separated from the tin melted by centrifugation. Residual tin adhering to the crystal surfaces was removed by a brief etch in dilute hydrochloric acid. Magnetic and transport measurements were carried out in a Quantum Design Physical Property Measurement System (PPMS). Prior to each measurement the sample was demagnetized by an oscillating-field degauss routine to eliminate remanent magnetic fields. Angle-dependent de Haas–van Alphen oscillations were recorded using a homemade sample holder that allowed the control of the field orientation with respect to the crystal axes.

3. Results and discussions

3.1.Crystal Structure and Characteristic Superconductivity

β-$IrSn_4$ has the well-known $MoSn_4$-type body-centered tetragonal structure. As illustrated in Fig.1(a), the layer of Sn atoms arranges into a Shastry-Sutherland lattice, such a distortion often gives rise to unusual physical phenomena and provides an attractive platform for exploring non-trivial topological states.[25] The Ir atoms form a simple square net and is sandwiched by two Sn layers, generating an Sn–Ir–Sn trilayer structure. These trilayers are stacked periodically along the *c*-axis, yielding a layered composite structure. The β-$IrSn_4$ single crystals were grown by the self-flux method, which effectively avoids contamination from extraneous elements. A photo of a typical

crystal with a well-defined square morphology was shown in the inset of Fig.1(b), consistent with its tetragonal crystal structure. To verify the chemical composition, scanning electron microscopy (SEM) coupled with energy-dispersive X-ray spectroscopy (EDS) was performed on the as-grown β-$IrSn_4$ crystals (Fig.S1). There are no extra peaks shown in the EDS spectrum and give a semi-quantitative stoichiometric of Ir: Sn ≈1: 4. The x-ray diffraction (XRD) patterns recorded on a single crystal (Fig.1(b)) displays only (00l) reflections, indicating a preferred orientation along the *c*-axis. Additionally, a sharp and well-defined Laue diffraction spot without extra or

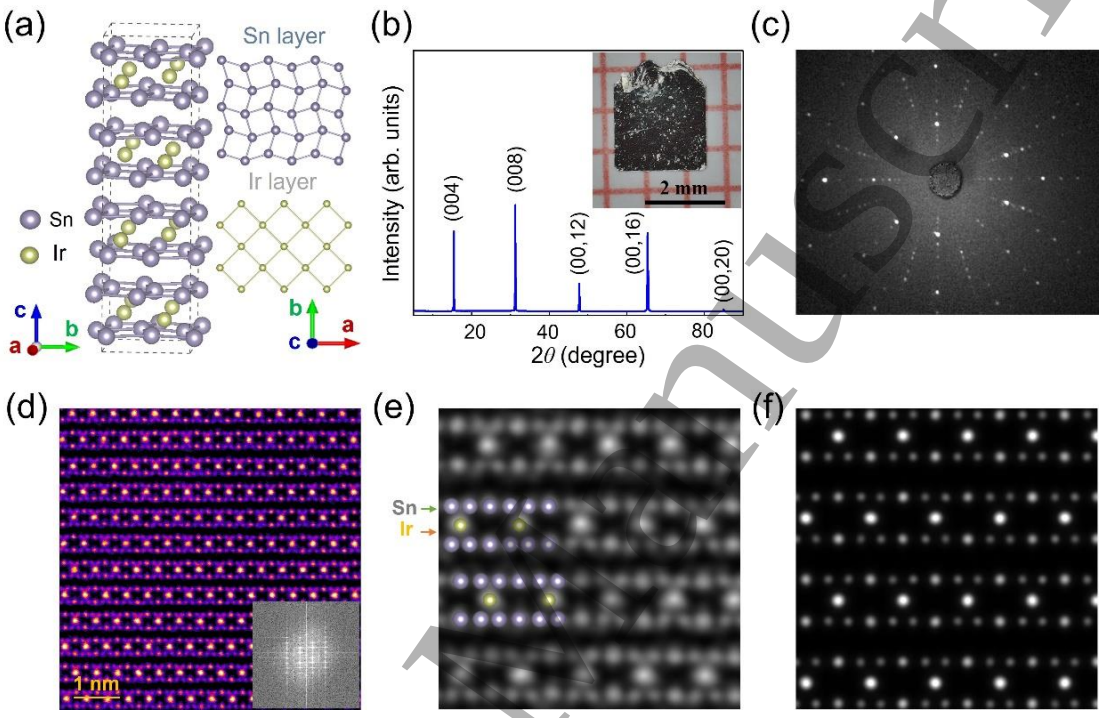

multiple sets of reflections shown in Fig.1(c), suggesting the high crystalline quality of the sample. To further confirm the crystal structure, the atomic-resolution high-angle annular dark-field scanning transmission electron microscopy (HAADF-STEM) was also conducted along the [011] direction (Fig.1(d)). A zoom-in Z-contrast projection with the crystallographic model superimposed in Fig.1(e), displays the perfect lattice of β-$IrSn_4$ without any discernible defects or impurity. A direct comparison between the experimental STEM micrograph (Fig.1(e)) and the simulated image generated from the β-$IrSn_4$ structural model (Fig.1(f)) shows an excellent match, confirming that the observed atomic arrangement is in quantitative agreement with the reported crystal structure.

Fig.1. Atomic structures and Transport analysis of the β-$IrSn_4$ crystal. (a) Schematic structure of β-$IrSn_4$ crystal with Ir atoms in light orange, Sn atoms in grey. The dashed lines represent a unit cell. (b) XRD pattern of the as-prepared β-$IrSn_4$ single crystal with the corresponding Miller indices (00*l*), indicating a preferred orientation along the *c*- axis. Inset is a photograph of the as-prepared β-$IrSn_4$ single crystal with a regular square morphology and sharp edges. The size of the crystal is over 2 mm * 2 mm. (c) Laue diffraction image of β-$IrSn_4$. (d) Atomically resolved HAADF image of a β-$IrSn_4$ single crystal cross-section after filter. The inset shows the FFT pattern. (e) HAADF image of the (011) plane along with the corresponding structural model. (f) Simulated atomic

structure.

3.2. De Haas-Van Alphen (dHvA) Oscillations

The magnetization of high-quality β-$IrSn_4$ single crystals was measured under low-temperature, high-magnetic-field conditions with the field applied along the crystallographic *c*-axis. The field dependence of magnetization (ΔM) at different temperatures are displayed in Fig. S2(a). β-$IrSn_4$ exhibits pronounced oscillations superimposed on a diamagnetic background under magnetic fields up to 9 T, resembling the behavior reported in β-$PtBi_2$, $PtSn_4$.[26, 27] After subtracting the quadratic background,[28, 29] the magnetization of β-$IrSn_4$ exhibits a pronounced multicomponent periodic behavior as a function of $1/B$, which is the character of dHvA oscillations. With increasing temperatures, the oscillations amplitude decays steadily and disappears completely around 30 K. To achieve a clearer separation of the different oscillatory components, the FFT method was employed, as shown in Fig.2(b). There are several fundamental frequencies: F_α = 9.0 T, F_β = 63 T, F_γ = 128 T, F_δ = 242 T, indicating that β-$IrSn_4$ possesses a complex Fermi-surface topology.

As the cornerstone of quantum-oscillations theory, Onsager's relation provides the link between the experimentally observed oscillations frequency F and the extremal cross-section area of the Fermi surface. It is expressed as $F = (\hbar/2\pi e)A_F$, where A_F is the extremal cross-section area of the Fermi surface perpendicular to the magnetic field, $\hbar$ is the reduced Planck constant, e is the elementary charge. Therefore, we can determine the four area are 0.00086 $Å^{-2}$, 0.00601 $Å^{-2}$, 0.0122 $Å^{-2}$, and 0.0231 $Å^{-2}$, corresponding to F_α, F_β, F_γ and F_δ, respectively.

According to the formula $A_F = \pi {k_F}^2$, the Fermi wave vectors (k_F) corresponding to each frequency can also be determined. Which is summarized in Table 1. The temperature and magnetic-field dependence of the oscillation amplitude is described by the L-K formula. When the Berry phase is taken into account, the oscillatory component of the magnetization can be written as

$$\Delta M \propto -\sqrt{B} R_T R_D R_S \sin\left[2\pi\left(\frac{F}{B} - \gamma - \delta\right)\right]$$

The oscillations amplitude of the dHvA signal can be described by three contributions that constitutes the three necessary conditions for observing quantum oscillations: the thermal damping term $R_T = \frac{2\pi^2 k_B T/\hbar\omega_c}{\sinh(2\pi^2 k_B T/\hbar\omega_c)}$, the scattering damping term $R_D = \exp\left(\frac{2\pi^2 k_B T_D}{\hbar\omega_c}\right)$ and the temperature and magnetic field independent Zeeman spin splitting term $R_S = \cos\left(\frac{\pi g \mu}{2}\right)$. Here, $\omega_c = \frac{eB}{m^*}$ and $\mu = \frac{m^*}{m_0}$, where m_0 and m^* are the free electron mass and effective mass of the charge carrier, respectively. The sine term corresponds to the phase factor, where γ equals to $\frac{1}{2} - \frac{\varphi_B}{2\pi}$ and φ_B

denotes the Berry phase. The phase shift δ, determined by the dimensionality of the Fermi surface, takes values of 0 for the 2D case and ±1/8 for the 3D case, respectively. Because multiple oscillatory components are superimposed in the raw signal, it is difficult to reliably extract the amplitude of a single frequency directly from the original oscillations. Therefore, we use the amplitudes obtained from the FFT spectra as a proxy for the oscillations amplitudes, which is consistent with the conventional data-analysis procedures adopted in the literature.[30] Firstly, By fitting the thermal damping of the oscillations, we can get effective cyclotron mass of 0.079m_e, 0.158m_e, 0.271m_e and 0.162 m_e for F_α, F_β, F_γ and F_δ, respectively. Notably, the F_α oscillations is associated with a particularly small effective mass, which is a feature commonly observed in systems with the Dirac-like linear dispersion, indicating the presence of potentially linear dispersive bands in β-$IrSn_4$. After determining the effective mass, the Fermi velocity can be further evaluated using the equation of $v_F = \frac{\hbar k_F}{m^*}$, and the calculated values are summarized in Table 1. The values of T_D are obtained from the slope of $\ln[\frac{\Delta M}{B^{1/2}R_T}]$ versus $\frac{1}{B}$ plots that are shown in Fig.S3 (a-d). It is worth noting that the waveform obtained for the δ oscillations cannot be cleanly isolated because of the contamination by components of other frequencies. Consequently, the oscillatory signal is analyzed using a sliding field-window Fourier transform, where the FFT is applied independently to successive magnetic-field intervals. For each FFT window, we assign a magnetic-field value equal to the harmonic meaning of the fields covered by that window. This procedure yields the magnetic-field dependence of the amplitude for each individual orbit. The main drawback of this method is that it precludes a subsequent Landau level index fit. The τ_q and μ_q of charge carriers are calculated using the relation $\tau_q = \frac{\hbar}{2\pi k_B T_D}$ and $\mu_q = \frac{e\hbar}{2\pi k_B m^* T_D}$, respectively. The parameters extracted and summarized in Table 1 exhibit pronounced differences among the four Fermi-pocket branches associated with the distinct oscillation frequencies. Notably, Table 1 highlights the exceptionally high quantum mobility of the charge carriers in β-$IrSn_4$, a characteristic that parallels the behavior reported for other topological electronic materials.[31-35]. Landau fans often be used to getting the Berry phase. Following the convention which assigns the peaks in ΔM to $n + \frac{1}{4}$ and valleys to $n - \frac{1}{4}$, where the Landau level index (LL index) n, which is an integer Berry phase is calculated from the intercept of the LL index versus $1/B$ plot, the Berry phase generally takes two values, 0 and π: for systems with $\varphi_B = 0$; for massless Dirac materials with the linear dispersion, $\varphi_B = \pi$, as shown in the Fig. 2(d). For F_β, the intercept of the Landau fan diagram is approximately 0.17, corresponding to a Berry-phase of $\varphi_B = 1.09\ \pi$ when $\delta = -1/8$. This result indicates that the Fermi surface associated with F_β is a non-trivial band topology with the three-dimensional character.

It is worth noting that, although the frequency F_γ is nearly twice F_β, these two branches originate from different extremal cross-sections of the Fermi surface rather than representing a fundamental frequency and its second harmonic. The conclusion is

supported by their distinct effective masses: F_β yields an effective mass of m^*=0.158 m_e, while F_γ corresponding to m^* = 0.271 m_e. If F_γ is the second harmonic of F_β, one would expect the two components to exhibit the same effective mass, which is not inconsistent with the experimentally observations.

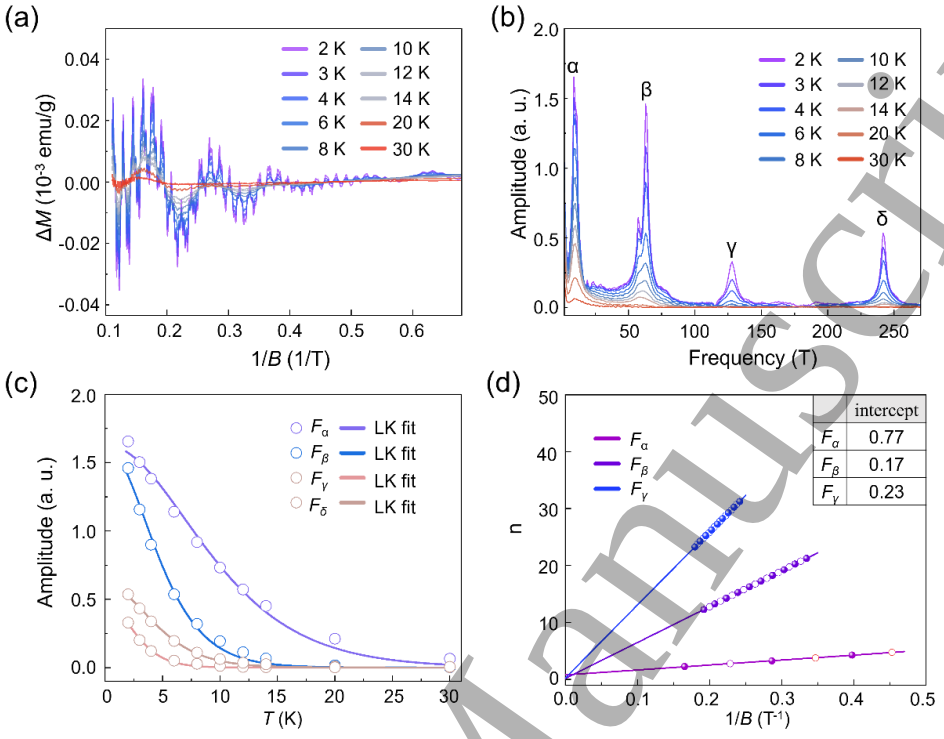

Fig. 2. Temperature dependence and FFT of dHvA oscillations in β-$IrSn_4$ for the $B \parallel c$-axis configuration. (a) Oscillations with subtracting background from the field- dependent magnetization of β-$IrSn_4$. The amplitude decreases with the increase of temperature and finally fades at ~30 K. (b) FFT of (a), showing four peaks in the low frequencies. (c) Temperature dependence of amplitude, extracted from (b). The solid line shows the best L-K fitting results. (d) The Landau level index (n) plot of the oscillations involves considering valley positions as integer indexes (n+1/4) and peak positions as half-integer indexes (n-1/4), following convention. The inset table in the upper-right corner lists the intercept values for each frequency component.

Table 1. The Fermi surface parameters obtained from dHvA oscillations analysis of $B \parallel c$-axis.

	F (T)	k_F (Å^{-1})	A_F (Å^{-2})	$m^*(m_e)$	v_F (ms^{-1})	T_D (K)	τ_q (10^{-13} s)	μ_q (cm^{2}V^{-1}s^{-1})	φ_B
α	9	1.7×10^{-2}	8.6×10^{-4}	0.079	2.5×10^5	3.90	3.12	0.69×10^4	0
β	63	4.4×10^{-2}	6.0×10^{-3}	0.158	3.2×10^5	0.94	13.0	1.44×10^4	π
γ	128	6.2×10^{-2}	1.2×10^{-2}	0.271	2.6×10^5	1.41	8.63	0.56×10^4	0
δ	242	8.6×10^{-2}	2.3×10^{-2}	0.162	6.1×10^5	3.53	3.44	0.37×10^4	/

The F, k_F, A_F, m^*, v_F, T_D, τ_q, μ_q stand for frequency, Fermi wave vector, cross-sectional area on the Fermi surface, effective mass, Fermi velocity, Dingel temperature, quantum scattering time, quantum mobility, respectively.

Furthermore, we also observed pronounced dHvA oscillations of β-$IrSn_4$, when the magnetic field is applied within the ab plane. The magnetization versus

magnetic-field curves for $B \parallel ab$ plane is shown in Fig. S2(b). Fig.3(a) shows the dHvA oscillations after subtracting the non-oscillatory background, extracted from Fig. S2(b). The magnetization continues to exhibit a well-defined periodicity as a function of $1/B$, analogous to the behavior observed for $B \parallel c$-axis. A larger number of frequencies is observed for the $B \parallel ab$ plane, indicating a more intricate Fermi-surface topology in this orientation. We performed a FFT analysis on the signal displayed in Fig.3(a) to extract the individual oscillatory components with a higher accuracy. As shown in Fig.3(b), the Fourier spectrum resolves six well-defined fundamental frequencies: $F_\xi = 7.0$ T, $F_\varepsilon = 17$ T, $F_\lambda = 24$ T, $F_\sigma = 42$ T, $F_\zeta = 76$ T and $F_\eta = 145$ T. Then we can calculate the area of F_ξ, F_ε, F_λ, F_σ, F_ζ and F_η are 0.00067 Å^{-2}, 0.00162 Å^{-2}, 0.00229 Å^{-2}, 0.00401 Å^{-2}, 0.00725Å^{-2}, and 0.0138 Å^{-2} respectively. Compared to the $B//c$ configuration, the $B//ab$-plane orientation exhibits a larger number of oscillations frequencies, most of which are located in the low-frequency regime, suggesting a more complex Fermi surface with multiple small extremal cross sections in the ab plane. The effective masses are extracted by fitting the thermal damping factor of L-K formula (Fig.3(c)), and the results are summarized in Table 2. The T_D values obtained from fitting are shown in Fig.S3(e-i). The Landau fan diagram is further performed to obtain the information of Berry phase. Overall, several small effective mass and non-trivial band topologies are observed for the $B//ab$ plane configuration, similar to those reported in Na_3Bi, $PtSn_4$, TaAs, ZrSiS.[18, 27, 36, 37]

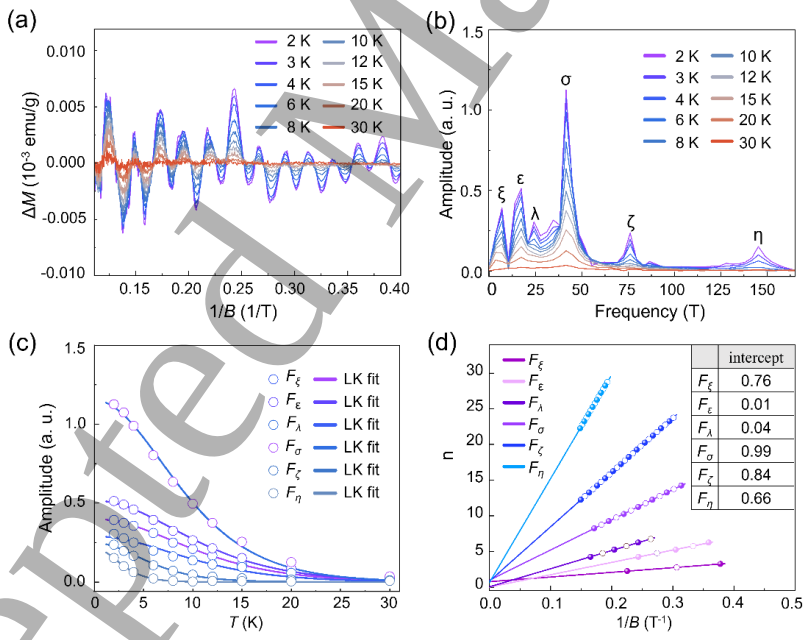

Fig. 3. Temperature dependence and FFT of dHvA oscillations in β-$IrSn_4$ study for the $B \parallel ab$ plane configuration. (a) Oscillations with the subtracting background from the field-dependent magnetization of β-$IrSn_4$ (Figure S2(b)). The amplitude decreases with the increase of temperature and finally fades at ~30 K. (b) FFT of (a), showing six peaks in the low frequencies. (c) Temperature dependence of amplitude, extracted from (b). The solid line shows the best L-K fitting results. (d) The Landau level index (n) plot of the oscillations involves considering valley positions as integer indexes (n+1/4) and peak positions as half-integer indexes (n-1/4), following convention. The inset

table in the upper-right corner lists the intercept values for each frequency component.

Table 2. The fermi surface parameters obtained from dHvA oscillations analysis of $B \parallel c$.

	F (T)	k_F (Å^{-1})	A_F (Å^{-2})	$m^*(m_e)$	v_F (ms^{-1})	T_D (K)	τ_q (10^{-13} s)	μ_q (cm^{2}V^{-1}s^{-1})	φ_B
ξ	7	1.5×10^{-2}	6.7×10^{-4}	0.071	2.4×10^{5}	4.70	2.58	0.64×10^{4}	0
ε	17	2.3×10^{-2}	1.6×10^{-3}	0.071	3.7×10^{5}	12.59	0.97	0.24×10^{4}	π
λ	24	2.7×10^{-2}	2.3×10^{-3}	0.074	4.2×10^{5}	4.56	2.67	0.63×10^{4}	π
σ	42	3.6×10^{-2}	4.0×10^{-3}	0.082	5.1×10^{5}	2.84	4.29	0.92×10^{4}	π
ζ	76	4.8×10^{-2}	7.3×10^{-3}	0.130	4.3×10^{5}	3.81	3.19	0.43×10^{4}	π
η	145	6.6×10^{-2}	1.4×10^{-2}	0.258	3.0×10^{5}	6.59	1.84	0.13×10^{4}	0

The F, k_F, A_F, m^*, v_F, T_D, τ_q, μ_q stand for frequency, fermi wave vector, cross-sectional area on the Fermi surface, effective mass, fermi velocity, Dingel temperature, quantum scattering time, quantum mobility, respectively.

3.3. Angular dependence of oscillations

To further investigate the geometry of the Fermi surface in β-$IrSn_4$, we systematically studied the angular evolution of the dHvA oscillations at 1.9 K (Fig.4(a)) the data recorded at the various field orientations have been vertically offset for visual clarity. The measurement configuration is illustrated in the inset of Fig.4(c), the θ is defined as the angle between the applied magnetic field and crystallographic c-axis. As the tilt angle θ increases, the oscillations amplitude decreases steadily, becoming almost imperceptible near 60°, and then gradually recovers when $\theta > 60°$. For a spherical Fermi surface, the extremal cross-sectional area probed by the magnetic field is isotropic, and the corresponding dHvA frequency should remain unchanged during the magnetic-field rotation. Consequently, the angle-dependent oscillations frequencies observed in β-$IrSn_4$ indicate the presence of multiple anisotropic Fermi-surface sheets. The FFT spectra of Fig.4(a) is presented in Fig.4(b), which provides a more convenient and quantitative analysis of the angular evolution of the Fermi-surface cross-sectional areas. Fig.4(c) summarizes the angular dependence of the observed oscillations frequencies, and the dashed lines represent fits using the relation $F(\theta) = F(0°)/cos(\theta)$. For F_α, the oscillations frequency gradually increases from 9 T for $\theta = 0°$ degree to 13 T for $\theta = 50°$, and undetectable once $\theta > 40°$. Importantly, the frequency can be well fitted by the formula $F_\alpha(\theta) = F_\alpha(0°)/\cos\theta$. In addition, F_β can be well fitted up to $\theta = 40°$ by using the formula $F_\beta(\theta) = F_\beta(0°)/cos\,\theta$ and the angular dependence of the F_ξ and F_ε can be well fitted up to $\theta = 60°\sim 90°$ by using the formula $F_j(\theta) = F_j(90°)/\cos(90° - \theta)$, j = σ or ε. These results indicate that, in β-$IrSn_4$, the Fermi-surface corresponding to the F_α, F_β, F_ξ, and F_ε possess the prolate ellipsoid or quasi-2D geometries. In addition, for F_δ, the frequency increases rapidly from 242 T at $\theta = 0°$ to 266 T at $\theta = 20°$. This pronounced evolution cannot be simply described by the above fitting formulas, indicating that the corresponding Fermi surface has a more complex

geometry, which calls for the further verification by theoretical calculations or angle-resolved photoemission spectroscopy (ARPES) experiments.

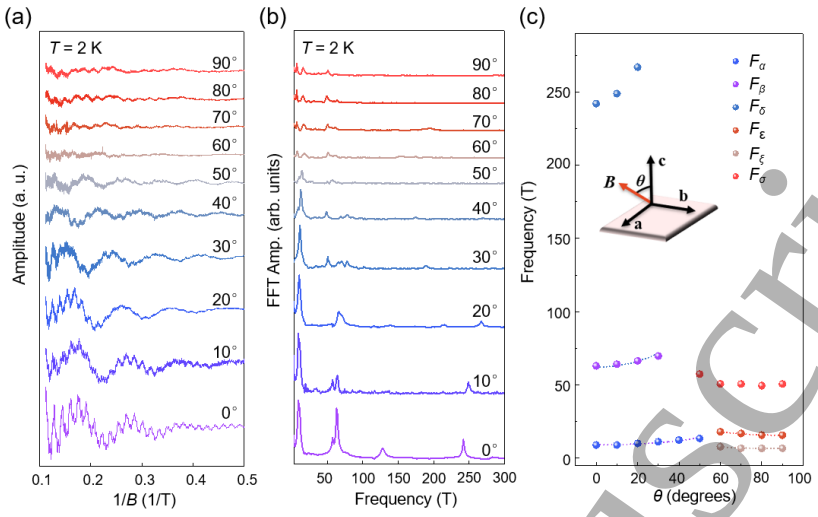

Fig. 4. (a) Background-subtracted oscillations patterns at different θ from the $B \parallel c$-axis to $B \parallel ab$ plane. (b) Field dependence of FFT amplitudes of dHvA oscillations at various field directions (θs) at T = 1.9 K. The data at different field directions has been shifted for clarity. (c) Angular dependence of oscillations frequencies F_α, F_β, F_δ, F_ε, F_ξ and F_σ. The inset shows a schematic illustration of the definition of θ. The dashed line is calculated from the formula $F_j(\theta) = F_j(90°) / \cos(90° - \theta)$, $j = \xi$ or ε; $F_i(\theta) = F_i(0°) / \cos\theta$(i = α or β).

4. Conclusion and perspectives

In summary, we have successfully grown high-quality β-$IrSn_4$ single crystals. Under high-field and low-temperature, clear de Haas–van Alphen quantum-oscillations are observed for both the $B \parallel c$-axis and $B \parallel ab$ plane. FFT analysis of the oscillatory component reveals four principal frequencies for $B \parallel c$-axis (F_α = 9.0 T, F_β = 63 T, F_γ = 128 T, F_δ = 242 T) and six principal frequencies for the $B \parallel ab$ plane (F_ξ = 7 T, F_ε = 17 T, F_λ = 24 T, F_σ = 42 T, F_ζ = 76 T, F_η = 145 T). These results demonstrate that β-$IrSn_4$ possesses the highly complex and anisotropic Fermi surface. Lifshitz–Kosevich analysis shows that the effective cyclotron mass located in the range 0.05~0.30 m_e, the very low effective mass points to a possible Dirac-like linear band dispersion in β-$IrSn_4$. Landau fan diagram analyses further yield Berry phases close to π for multiple oscillations branches (F_β, F_ε, F_λ, F_σ, F_ζ), indicating the presence of nontrivial topological bands. Angle-dependent dHvA measurements reveal multiple cylindrical or ellipsoidal Fermi surface sheets, together with additional pockets of more complex geometry. Overall, systematic magnetic measurements and quantum oscillations studies elucidate the complex Fermi surface geometry and signatures of the non-trivial band structure of this system, establishing it as a valuable experimental platform for investigating the interplay between the superconductivity and band topology.

5. Acknowledgments

The work is supported by grants from the National Key Research and Development Projects of China (2022YFA1204100), the National Natural Science Foundation of China (62488201), the Innovation Program of Quantum Science and

Technology (2021ZD0302700) and the China Postdoctoral Science Foundation (E5BK081).

References

[1] Armitage N P, Mele E J and Vishwanath A 2018 *Reviews of Modern Physics* **90** 0034

[2] Reddy A P, Alsallom F, Zhang Y, Devakul T and Fu L 2023 *Physical Review B* **108** 085117

[3] Deng Y J, Yu Y J, Shi M Z, Guo Z X, Xu Z H, Wang J, Chen X H and Zhang Y B 2020 *Science* **367** 895

[4] Liu Z K, Jiang J, Zhou B, Wang Z J, Zhang Y, Weng H M, Prabhakaran D, Mo S K, Peng H, Dudin P, Kim T, Hoesch M, Fang Z, Dai X, Shen Z X, Feng D L, Hussain Z and Chen Y L 2014 *Nature Materials* **13** 677

[5] Banerjee N, Bell C, Ciccarelli C, Hesjedal T, Johnson F, Kurebayashi H, Moore T A, Moutafis C, Stern H L, Vera-Marun I J, Wade J, Barton C, Connolly M R, Curson N J, Fallon K, Fisher A J, Gangloff D A, Griggs W, Linfield E, Marrows C H, Rossi A, Schindler F, Smith J, Thomson T and Kazakova O 2025 *Appl Phys Rev* **12** 041328

[6] Hasan M Z and Kane C L 2010 *Reviews of Modern Physics* **82** 3045

[7] Wang D F, Kong L Y, Fan P, Chen H, Zhu S Y, Liu W Y, Cao L, Sun Y J, Du S X, Schneeloch J, Zhong R D, Gu G D, Fu L, Ding H and Gao H J 2018 *Science* **362** 333

[8] Xu S Y, Belopolski I, Alidoust N, Neupane M, Bian G, Zhang C L, Sankar R, Chang G Q, Yuan Z J, Lee C C, Huang S M, Zheng H, Ma J, Sanchez D S, Wang B K, Bansil A, Chou F C, Shibayev P P, Lin H, Jia S and Hasan M Z 2015 *Science* **349** 613

[9] Pariari A K, Sharma R O, Balal M, Hücker M, Das T and Barman S R 2025 *Advanced Functional Materials* **35** 2412515

[10] Han L X S, Shi X B, Jiao J L, Yu Z H, Wang X, Yu N, Zou Z Q, Ma J, Zhao W W, Xia W and Guo Y F 2022 *Chinese Physics Letters* **39** 067101

[11] Xing Y, Wang H, Li C K, Zhang X, Liu J, Zhang Y W, Luo J W, Wang Z Q, Wang Y, Ling L S, Tian M L, Jia S, Feng J, Liu X J, Wei J and Wang J 2016 *Npj Quantum Materials* **1** 16605

[12] Lévy F, Sheikin I, Grenier B, Marcenat C and Huxley A 2009 *J Phys-Condens Mat* **21** 16

[13] Diaz J, Wang K, Straquadine J, Putzke C, Yang Q, Yan B H, Bud'ko S L, Canfield P C and Moll P J W 2024 *Nature Communications* **15** 2041

[14] Shen D, Kuo C N, Yang T W, Chen I N, Lue C S and Wang L M 2020 *Communications Materials* **1** 2662

[15] Zhu W, Song R, Huang J, Wang Q-W, Cao Y, Zhai R, Bian Q, Shao Z, Jing H, Zhu L, Hou Y, Gao Y-H, Li S, Zheng F, Zhang P, Pan M, Liu J, Qu G, Gu Y, Zhang H, Dong Q, Huang Y, Yuan X, He J, Li G, Qian T, Chen G, Li S-C, Pan M and Xue Q-K 2023 *Nature Communications* **14** 7012

[16] Xu C Q, Li B, Zhang L, Pollanen J, Yi X L, Xing X Z, Liu Y, Wang J H, Zhu Z W, Shi Z X, Xu X F and Ke X 2021 *Physical Review B* **104** 12

[17] Ahmad N, Shimada S, Hasegawa T, Suzuki H, Afzal M A, Nakamura N, Higashinaka R, Matsuda T D and Aoki Y 2024 *Journal of the Physical Society*

of Japan **93** 044706
[18] Hu J, Tang Z J, Liu J Y, Zhu Y L, Wei J and Mao Z Q 2017 *Physical Review B* **96** 045127
[19] Potter A C, Kimchi I and Vishwanath A 2014 *Nature Communications* **5** 5161
[20] He L P, Hong X C, Dong J K, Pan J, Zhang Z, Zhang J and Li S Y 2014 *Physical Review Letters* **113** 246402
[21] Fu Y, Zhao N N, Chen Z, Yin Q W, Tu Z J, Gong C S, Xi C Y, Zhu X D, Sun Y P, Liu K and Lei H C 2021 *Physical Review Letters* **127** 207002
[22] Nakamura N, Yanuma A, Chiba Y, Omura R, Higashinaka R, Harima H, Aoki Y and Matsuda T D 2023 *Journal of the Physical Society of Japan* **92** 034701
[23] Nordmark E L, Wallner O and Häussermann U 2002 *Journal of Solid State Chemistry* **168** 34
[24] Tran V H, Bukowski Z, Wisniewski P, Tran L M and Zaleski A J 2013 *J Phys-Condens Mat* **25** 155701
[25] Wu H, Hallas A M, Cai X C, Huang J W, Oh J S, Loganathan V, Weiland A, McCandless G T, Chan J Y, Mo S K, Lu D H, Hashimoto M, Denlinger J, Birgeneau R J, Nevidomskyy A H, Li G, Morosan E and Yi M 2022 *Npj Quantum Materials* **7** 31
[26] Bavaro E F, Castro J, Vildosola V, Facio J I and Correa V F 2025 *Physical Review B* **112** 245136
[27] Mun E, Ko H, Miller G J, Samolyuk G D, Bud'ko S L and Canfield P C 2012 *Physical Review B* **85** 035135
[28] Dong Z X, Shi L, Wang B, Huo M W, Huang X, Huang C X, Ma P Y, Zhang Y W, Shen B and Wang M 2024 *Chinese Physics B* **33** 107102
[29] Zhang Y H, Yi X W, Zhao Z, Liu J L, Xu A N, Li D, Lu Z Y W, Liu Y, Lu J H, Zhang H, Chen H, Li S L, Liu Z Y, Cheng J G, Su G, Yang H T, Dong X L, Gao H J and Zhao Z X 2025 *Chinese Physics B* **34** 077107
[30] Aoki D, Homma Y, Harima H and Sheikin I 2025 *Physical Review B* **111** 035155
[31] Singha R, Pariari A K, Satpati B and Mandal P 2017 *P Natl Acad Sci USA* **114** 2468
[32] Hu J, Tang Z J, Liu J Y, Liu X, Zhu Y L, Graf D, Myhro K, Tran S, Lau C N, Wei J and Mao Z Q 2016 *Physical Review Letters* **117** 016602
[33] Han X, Pi H Q, Yan D Y, Zhang R H, Li Y, Wang X, Dun Z, Wang Z J, Feng H L, Wu Q S and Shi Y G 2023 *Physical Review B* **108** 2469
[34] Hu J, Xu S Y, Ni N and Mao Z Q 2019 *Annu Rev Mater Res* **49** 207
[35] Sarkar S, Sadhukhan P, Singh V K, Gloskovskii A, Deguchi K, Fujita N and Barman S R 2021 *Physical Review Research* **3** 2643
[36] Liu Z K, Zhou B, Zhang Y, Wang Z J, Weng H M, Prabhakaran D, Mo S K, Shen Z X, Fang Z, Dai X, Hussain Z and Chen Y L 2014 *Science* **343** 864
[37] Huang S M, Xu S Y, Belopolski I, Lee C C, Chang G Q, Wang B K, Alidoust N, Bian G, Neupane M, Zhang C L, Jia S, Bansil A, Lin H and Hasan M Z 2015 *Nature Communications* **6 2041**

Supporting Information

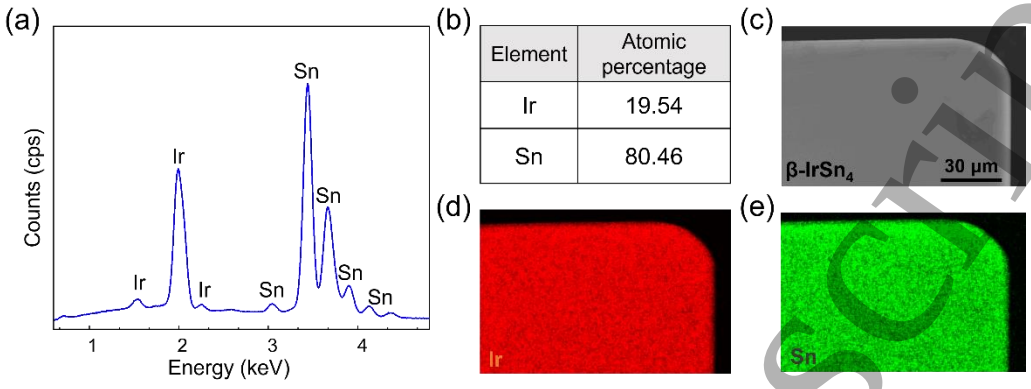

Fig. S1. EDS spectrum and elements mapping image of β-$IrSn_4$. (a) The elemental analysis performed using SEM-EDS. (b) EDS collected in multiple regions showing the chemical composition of Ir: Sn close to 1:4. (c) The SEM image of β-$IrSn_4$ single crystal grown by the self-flux method. (d, e) SEM-EDX elemental mapping of Ir, Sn, respectively.

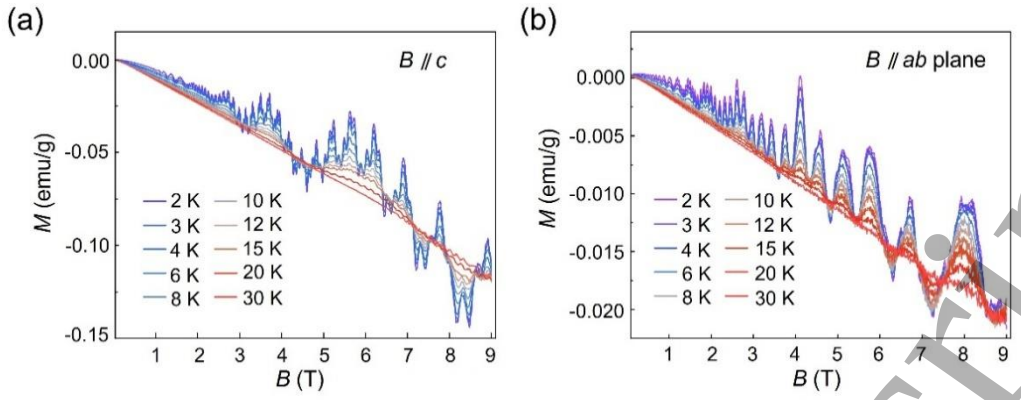

Fig. S2. (a) Isothermal magnetization of β-$IrSn_4$ single crystal with applied magnetic field along the *c* axis (*B*//*c*). (b) Isothermal magnetization of β-$IrSn_4$ single crystal with applied magnetic field parallel to *ab* plane (*B*//*ab* plane).

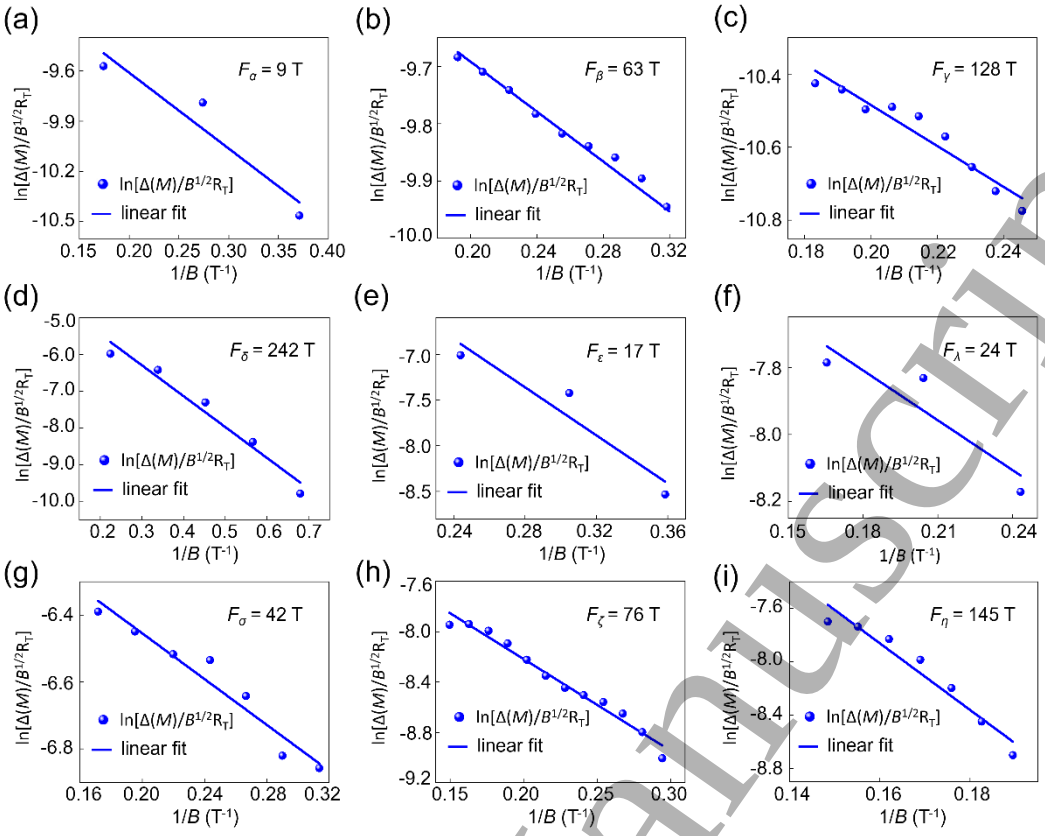

Fig. S3. (a-d) Dingle temperature plots of the four FFT frequencies 9 T, 63 T, 128 T and 242 T, respectively, in the dHvA oscillations study for the $B \parallel c$-axis configuration. (e-i) Dingle temperature plots of the five FFT frequencies 17 T, 24 T, 42 T 76 T and 145 T, respectively in the dHvA oscillations study for the $B \parallel ab$ plane configuration.